Sublattice-selective inversion of dual- and multiple-scattering He^+ survival in binary collision approximation simulations of α-Al_2O_3: A comparative study with α-SiO_2, GaN, and 3*C*-SiC

A. S. Ashirov *

Department of Physics, Urgench State University, 220100 Urgench, Uzbekistan

(Received 16 May 2026; revised 12 August 2026; accepted 14 August 2026; published 1 September 2026)

The He^+ charge-state survival probability sets the absolute scale of quantitative low-energy ion scattering (LEIS), and a recent $CaSiO_3$ study [J. Brötzner *et al.*, Phys. Rev. B **113**, 075405 (2026)] has shown that this probability depends on whether the backscattered trajectory involves one, two, or several collisions—suggesting that quantitative analysis ought to discriminate by collision history. How far this regime hierarchy generalizes is, however, an open question. This is addressed through scattering-regime-resolved binary collision approximation (BCA) simulations of He^+ at 1–3 keV under grazing incidence ($\psi = 22^\circ$) for four crystallographically distinct targets: α-quartz SiO_2, corundum α-Al_2O_3, wurtzite GaN, and zincblende 3C-SiC. The calculations combine pair-specific Nordlund-Lehtola-Hobler potentials, position-dependent electronic stopping, Debye thermal vibrations, and a velocity-dependent Hagstrum kernel; statistically converged trajectory ensembles were accumulated for the high-statistics analysis. For α-SiO_2, GaN, and 3*C*-SiC, the standard ordering $\langle P^+\rangle_s > \langle P^+\rangle_d > \langle P^+\rangle_m$ is recovered, with single-to-multiple contrast $R_{s/m} \approx 1.5$–2.2. Corundum exhibits a qualitatively different behavior. When the backscattered ensemble is decomposed by the chemical identity of the final-collision atom, dual-scattering trajectories ending on the dominant Al sublattice show a charge survival *below* that of multiple-scattering ones at all five investigated energies. The sublattice-resolved inversion is highly significant—19.7σ at 1 keV in the pooled three-seed ensemble, weakening monotonically to 3.7σ at 3 keV—and reproduces across three independent random seeds (per-seed significance $10.9-11.7\sigma$ at 1 keV). Because Al-ending trajectories make up 79%–83% of the backscattered population, the inversion also persists in the integrated signal ($P_d/P_m = 0.59$–0.80) despite the oppositely ordered minority O sublattice. The inversion is robust to a $\pm 30\%$ variation of the Hagstrum velocity parameter and survives detector-window selection. Tracking the recorded collision pairs reveals the cause: two Al atoms in the same atomic plane make up 52%–72% of the dual events in α-Al_2O_3 (the fraction rising toward low energy; $\langle|\Delta z|\rangle = 0.29$ Å, small compared with the interlayer spacing), clustering at three characteristic in-plane separations of $\approx$2.6, 4.7, and 7.1 Å that correspond to the first, second, and fourth Al-Al neighbor shells of corundum. Such a near-grazing intralayer trajectory remains within the high-density surface region considerably longer than a steep multicollision excursion, which enhances neutralization at the second encounter. These results indicate that quantitative regime-resolved charge-fraction analysis in He^+ LEIS, while suggested by recent measurements on $CaSiO_3$, must in general account for lattice topology and sublattice composition rather than collision count alone.

DOI: 10.1103/yx82-j8nn

I. INTRODUCTION

Among surface analytical methods, low-energy ion scattering (LEIS) remains unmatched in its sensitivity to the topmost atomic layers [1–4]. The principle is straightforward: a keV-range noble-gas ion undergoes a single large-angle binary collision with a target atom, and the energy lost in that encounter is fixed by the kinematics of the colliding pair. Mass identification then follows directly from the recorded backscatter energy, with monolayer resolution that few other techniques can match. Routine applications today range from ultrathin oxide overlayers and plasma-modified surfaces to compound semiconductors and supported catalyst nanoparticles.

Quantitative analysis with He projectiles is, however, complicated by the charge-state problem. Only the charged fraction of the backscattered flux reaches the electrostatic analyzer, and that fraction is set by a delicate competition between resonant and Auger neutralization processes. It depends on the projectile velocity, the exit angle, the local electronic structure of the surface, and—crucially—the time the ion spends within the high-density electron cloud near the solid [5–10]. The conversion from detected He^+ intensity to absolute surface concentration is therefore not universal. An effective charge fraction calibrated on one projectile–target combination cannot be carried over to another without correction, and this single fact accounts for much of the residual quantitative uncertainty in routine LEIS analysis.

*Contact author: atabek.ashirovs@gmail.com

Published by the American Physical Society under the terms of the Creative Commons Attribution 4.0 International license. Further distribution of this work must maintain attribution to the author(s) and the published article's title, journal citation, and DOI.

In practice, one usually assigns a single effective charge fraction ξ to each element and calibrates it against a reference compound. The approximation is convenient but crude. Any given surface peak in a real spectrum can be populated by direct single backscattering, by a dual collision linking two near-surface atoms, or by a sequence of multiple collisions reaching several layers below the topmost plane. These trajectory classes differ in path length, in penetration depth, in accumulated inelastic loss, and in the velocity with which the ion eventually escapes the surface. There is no *a priori* reason that they should share a common neutralization probability, and accumulating evidence suggests that they do not.

The $CaSiO_3$ study of Brötzner *et al.* [11] put this intuition on a quantitative footing. They reported that the He^+ charge fractions associated with single and dual scattering exceed the multiple-scattering value by close to an order of magnitude, with a clean ordering $P^+_{\text{single}} > P^+_{\text{dual}} > P^+_{\text{multiple}}$, and they attributed this to the longer effective transit of multicollision ions through the surface electron density. The result is striking. It also raises a question their measurement could not, by itself, settle: is this hierarchy a generic property of multicomponent insulators and semiconductors, or is it tied to the particular electronic structure of calcium silicate? Trajectory-based calculations of grazing-incidence scattering from oxides [12–16] provide the methodological tools to address this question, but a comparative regime-resolved analysis across material classes has been missing.

The question is not academic. SiO_2 and Al_2O_3 are workhorse dielectric and passivation layers in microelectronics; GaN and SiC underpin much of modern high-power, high-frequency, and radiation-hard device technology, where stoichiometry and near-surface disorder shape device performance directly. Each of these surfaces has been studied individually with LEIS and related ion-scattering techniques [15–21], but a side-by-side regime-resolved comparison across material classes has not, to the author's knowledge, been attempted.

That comparison is attempted here. Four crystallographically distinct targets were chosen to span the principal material classes encountered in LEIS practice: α-quartz SiO_2 (representative oxide, moderately open framework), corundum α-Al_2O_3 (dense oxide with an hcp anion sublattice), wurtzite GaN (wide-band-gap nitride), and zincblende *3C*-SiC (wide-band-gap carbide). The simulations are carried out within the binary collision approximation (BCA) using pair-specific Nordlund-Lehtola-Hobler potentials [22–24], position-dependent electronic stopping that follows recent evidence for trajectory-dependent energy loss [15,16], and a velocity-dependent Hagstrum-type neutralization kernel [5,8,25–27]. For every backscattered trajectory, the collision count, charge survival, maximum penetration depth, accumulated inelastic loss, and chemical identity of the atom involved in the final collision are recorded.

The principal finding is that the regime hierarchy of Brötzner *et al.* is not universal. For α-SiO_2, GaN, and *3C*-SiC, the standard ordering survives, with single-to-multiple contrast $R_{s/m} \approx 1.5$–2.2 across the studied energy range—weaker than in $CaSiO_3$ but qualitatively the same. Corundum is different. On the dominant Al sublattice, dual-scattering trajectories exhibit a *lower* charge survival than multiple-scattering ones, by up to a factor of three, at up to 19.7σ (pooled three-seed ensemble at 1 keV; 10.9-11.7σ per individual seed), a result reproduced across three independent random seeds. On the O sublattice, the conventional ordering returns. Tracking the trajectory geometries reveals the underlying mechanism: in corundum a He^+ projectile undergoing a dual collision is most likely to encounter two Al atoms within the same *a*-*b* plane, separated laterally by the characteristic Al-Al neighbor distances of the corundum lattice and vertically by an amount small compared with the interlayer separation. Such a near-grazing intralayer trajectory dwells in the high-density electron region of the surface for an unusually long time—longer than the deeper but steeper multicollision excursions—and the neutralization probability rises accordingly.

The paper is organized as follows. Section II sets out the BCA framework, target structures, interatomic potentials, the electronic-stopping and neutralization treatments, and the trajectory classification. Section III presents the regime-resolved charge fractions for all four targets, identifies the α-Al_2O_3 anomaly, demonstrates its robustness against parameter and geometry choices, and resolves it microscopically through sublattice and pair-geometry decompositions. Section IV places the result in the broader context of quantitative LEIS analysis and proposes a regime-by-sublattice decomposition $\xi_{\alpha,k}$ of the effective charge fractions. Section V summarizes the main implications.

II. COMPUTATIONAL MODEL

A. BCA framework

The simulations were performed with a custom Python implementation of the binary collision approximation in the Robinson-Torrens lineage [28–30]. The projectile trajectory is built up from a sequence of independent two-body collisions, each separated by a free flight in the screened lattice field; between collisions, the ion loses energy continuously through electronic stopping. For keV-range projectiles, the approximation is well-suited: large-angle elastic scattering dominates, and the trajectory can be resolved at the level of individual binary encounters with no need for many-body terms. For each ion, the following were recorded: the position (x, y, z) and the unit propagation vector (L, M, N) at every collision, the instantaneous kinetic energy E, the running collision count k, the maximum penetration depth, the accumulated inelastic loss $\Sigma\Delta E_{\text{inel}}$, the chemical identity of the final-collision atom, and the spatial coordinates of the first three encounters along the trajectory.

A trajectory was flagged as backscattered when it crossed the exit plane $z = z_{\text{exit}} = 1.0$ Å with residual kinetic energy above 100 eV. Ions whose path leaves the supercell laterally before that plane is reached require special handling. A straight-line extrapolation to the exit plane is applied, and the result is accepted only if the projected lateral displacement $|\mathbf{r}_{\text{lat}}| = t_{\text{exit}}\sqrt{1 - N^2}$ remains within the supercell footprint. The criterion is geometric and unbiased: at grazing exit angles ($N \to 0$, large $|\mathbf{r}_{\text{lat}}|$) ions extrapolated beyond the supercell are discarded, while at steep exit angles ($N \to 1$, small $|\mathbf{r}_{\text{lat}}|$) all reasonable trajectories are correctly retained.

B. Target structures

Four crystalline targets were chosen to span the principal LEIS-relevant material classes.

(1) α-quartz **SiO_2** (space group $P3_221$, $a = 4.913$ Å, $c = 5.405$ Å, $\rho = 2.65$ g/cm^3). α-quartz is the thermodynamically stable SiO_2 polymorph at room temperature and is structurally closer to amorphous SiO_2 surfaces than the open-framework β-cristobalite phase that has occasionally been used in BCA work. Its higher density also damps the spurious channeling that hampers β-cristobalite simulations under grazing incidence.

(2) Corundum **α-Al_2O_3** ($R\bar{3}c$, $a = 4.760$ Å, $c = 12.99$ Å, $\rho = 3.99$ g/cm^3). The structure is built from an hcp oxygen sublattice with two-thirds of the octahedral interstices occupied by Al—a detail that turns out to be central to the results below.

(3) Wurtzite GaN ($P6_3mc$, $a = 3.189$ Å, $c = 5.185$ Å), in the Ga-terminated (0001) orientation.

(4) Zincblende *3C*-SiC ($F\bar{4}3m$, $a = 4.360$ Å), chosen as the most isotropic SiC polytype. The technologically more common 4H and 6H polytypes are expected to behave similarly because the local atomic packing is comparable; quantitative shifts due to stacking-fault rumpling cannot, however, be excluded.

The surface was treated as an ideal crystalline termination without reconstruction. Thermal disorder was applied as isotropic Gaussian random displacements of the target atoms, the same one-dimensional root-mean-square amplitude being assigned independently to each Cartesian component. The element-dependent room-temperature amplitudes are Si: 0.065 Å, O: 0.085 Å, Al: 0.065 Å, Ga: 0.070 Å, N: 0.070 Å, and C: 0.050 Å, typical of room-temperature Debye-Waller displacement scales for these species (∼0.05–0.09 Å); the connection to the Debye-Waller B factor is $B = 8\pi^2\langle u_x^2\rangle$ [31]. No temperature scan is performed in this work: the values are used as fixed 300 K disorder parameters. The supercell size was chosen adaptively for the incidence geometry so that the ion encounters atoms over the full extent of its trajectory; for the $\psi = 22^\circ$ grazing configuration used throughout, the supercell extends roughly 50 Å laterally and 36 Å in depth.

C. Interatomic potentials and energy loss

Elastic scattering was treated using the pair-specific repulsive potentials of the Nordlund-Lehtola-Hobler (NLH) tabulation [22–24], with the published erratum corrections to the He-Si and He-O screening parameters applied. The NLH potentials abandon the universal-screening assumption of the Ziegler-Biersack-Littmark (ZBL) form [30], which matters here: the effective screening for a light He projectile differs appreciably from that of heavier noble gases, and ZBL underestimates the small-impact-parameter scattering angles by enough to change backscatter yields by tens of percent. For each collision with impact parameter p and projectile energy E, the center-of-mass scattering angle was obtained by numerical integration of the classical scattering integral, and laboratory-frame quantities were then computed from two-body kinematics with a local inelastic-loss correction.

Electronic stopping between collisions was applied as a continuous energy-loss term $S_e(v, \rho)$ depending on the local position of the trajectory relative to atomic rows. The position dependence is motivated by recent experimental evidence that channeled trajectories experience reduced electronic energy loss [15,16]. The accumulated inelastic loss $\Sigma\Delta E_{\mathrm{inel}}$ reported below contains both the local collision-associated component and the continuous between-collision contribution.

D. Charge-state survival kernel

The probability that a backscattered He projectile exits the surface in a charged state was evaluated through a velocity-dependent Hagstrum-type kernel,

$$P^+ = \exp\left(-\frac{v_0}{v_\perp}\right), \tag{1}$$

with v_0 a characteristic neutralization velocity and $v_\perp$ the component of the exit velocity perpendicular to the surface, constructed from the final kinetic energy and the exit polar angle. Slow ions and ions leaving at near-grazing exit angles spend more time in the high-density electron region; their survival probability is correspondingly low. The form is consistent with the well-established picture of the He^+ charge-state problem in LEIS [5,8,25–27].

The base calculations used $v_0 = 3.3 \times 10^5$ m/s for the two oxides (α-SiO_2 and α-Al_2O_3) and $v_0 = 3.0 \times 10^5$ m/s for the wide-band-gap semiconductors (GaN and 3*C*-SiC). Crucially, the same v_0 was applied to all scattering regimes within a given material; no regime dependence is built into the kernel. The sensitivity of the results to this choice is examined in Sec. III D through an explicit ±30% scan.

Equation (1) should be read as an effective trajectory-level kernel rather than a microscopic description of every charge-exchange channel. More refined treatments that include explicit close-collision reionization and Auger pathways [9,25,27] would alter the absolute P^+ values, but the regime *ordering* reported below proves to be independent of the specific v_0 value within ±30% (see Sec. III D). The conclusions are not tied to a particular kernel parameter.

E. Scattering-regime classification

Following Brötzner *et al.* [11], every backscattered trajectory was classified by its collision count k,

$$\text{single} : k = 1, \quad \text{dual} : k = 2, \quad \text{multiple} : k \geqslant 3.$$

The classification was applied as a post-processing operation; it has no influence on ion propagation. For each material, energy, and regime, the following were computed: the regime-averaged survival probability $\langle P^+\rangle_r = N_r^{-1}\sum_{i\in r} P_i^+$, the regime-averaged maximum penetration depth, the mean inelastic loss, and the distribution of final-collision atoms. The single-to-multiple contrast is defined as $R_{s/m} = \langle P^+\rangle_{\mathrm{single}}/\langle P^+\rangle_{\mathrm{multiple}}$.

F. Simulation conditions

Calculations were carried out at five incident energies, $E_0 = 1.0$, 1.5, 2.0, 2.5, and 3.0 keV. The geometry was grazing incidence with polar angle $\psi = 22^\circ$ measured from the surface and azimuth $\xi = 0^\circ$ aligned with the principal axis of each crystal, representative of the grazing-incidence

ESA-LEIS geometries used in related experimental studies of compound surfaces [8,15,16]. The detector was modeled as a ring at $\theta_{\rm det} = 136^\circ$ between incident and detected directions, with half-acceptance $\pm 5^\circ$ for the production runs and $\pm 15^\circ$ for the wide-window statistics check. The four-material survey (Secs. III A–III B) used $N = 20\,000$ trajectories per seed at each material-energy point (three independent seeds). The α-Al_2O_3 anomaly was run at higher statistics, $N = 50\,000$ trajectories per seed. All of the α-Al_2O_3 analyses—the regime-resolved survival (Sec. III C), the v_0 and detector robustness checks (Sec. III D), the sublattice decomposition (Sec. III E), and the trajectory-topology analysis (Sec. III F)—are post-processing of the same three-seed production ensembles. Statistical errors quoted in the tables and figures are the standard error of the mean over independent trajectories within each regime ($eP_r = \sigma_{P,r}/\sqrt{N_r}$); the significance of the $P_m - P_d$ contrast is computed as the ratio of the difference to the quadrature sum of the two errors. Because every production point is itself run with three independent seeds, the seed-to-seed reproducibility of the anomaly is reported directly in Sec. III D. All simulations were run single-threaded on a single desktop CPU core (the code is not parallelized); a single α-Al_2O_3 point ($N = 50\,000$) takes on average about 2.7 h, so that the full production (three seeds, five energies, four materials) amounts to roughly 65 core-hours in total.

III. RESULTS

A. Backscattered yield and energy dependence

Figure 1 collects the integrated backscatter yield for the four targets as a function of incident energy. The decrease with energy is monotonic on a semilogarithmic scale and spans the same order-of-magnitude range across all four materials: 11.9% → 1.8% for α-SiO_2, 17.1% → 1.9% for α-Al_2O_3, 15.1% → 3.1% for GaN, and 20.7% → 2.0% for 3*C*-SiC over the 1–3 keV interval. These values are typical for grazing-incidence ESA-LEIS [2,8] and provide the reference context in which the regime-resolved analysis below should be read.

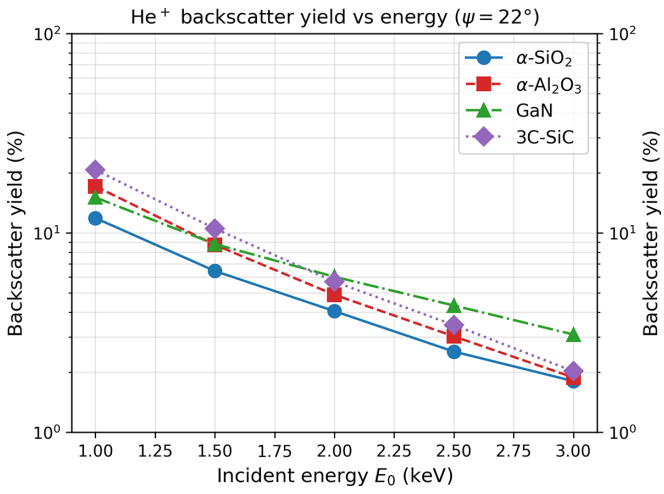


FIG. 1. Backscatter yield as a function of incident He^+ energy for α-SiO_2, α-Al_2O_3, GaN, and 3*C*-SiC at grazing incidence ($\psi = 22^\circ$). The yield is shown on a semilogarithmic scale to highlight the monotonic decrease with energy across all four targets. The right-hand axis mirrors the left; both scales are logarithmic and span 10^0% to 10^2%.

As one would expect, the denser targets (α-Al_2O_3 and 3*C*-SiC) deliver the highest low-energy yields, reflecting their higher density of near-surface scattering centers. α-SiO_2 sits at the bottom of the four throughout the energy range. It is worth noting that the choice of α-quartz over β-cristobalite as the SiO_2 representative is essential: in the same geometry, the β-cristobalite framework leaks ions through its open Si–O–Si channels, producing yields nearly an order of magnitude smaller than those of any real SiO_2 surface.

B. Regime hierarchy in α-SiO_2, GaN, and 3*C*-SiC

Figure 2 presents the regime-resolved mean He^+ survival probability $\langle P^+ \rangle$ versus incident energy for the four targets. A common trend stands out: $\langle P^+ \rangle$ rises with E_0 in every panel, as expected from the velocity dependence of Eq. (1). The ordering of the three regimes, however, is not the same in every material.

For three of the four materials—α-SiO_2, GaN, and 3*C*-SiC—the standard hierarchy

$$\langle P^+ \rangle_{\rm single} > \langle P^+ \rangle_{\rm dual} > \langle P^+ \rangle_{\rm multiple} \tag{2}$$

is observed at all five energies. The single-to-multiple contrast lies in the range $R_{s/m} = 1.5$–1.7 for α-SiO_2, 1.7–1.9 for GaN, and 1.9–2.2 for 3*C*-SiC. These values are weaker than the near-order-of-magnitude contrast reported for $CaSiO_3$ [11], but the qualitative ordering of Eq. (2) is preserved. The reduction in contrast is internally consistent with the materials examined here: the wide-band-gap semiconductors are less ionic than $CaSiO_3$, and α-quartz has a denser anion sublattice than the open silicate network of $CaSiO_3$. Both effects work in the same direction—they reduce the path-length difference between single, dual, and multiple trajectories that drives the regime contrast in the first place.

The energy dependence is what one expects from Eq. (1): higher-energy ions exit faster, with larger $v_\perp$, and survive better. More importantly, the regime hierarchy persists across the entire energy range, which means the ordering is set by the underlying trajectory topology—path length, depth, inelastic loss—rather than by velocity alone.

C. Anomalous regime ordering in α-Al_2O_3

Corundum exhibits qualitatively different behavior. As shown in the upper-right panel of Fig. 2, the three regime curves run nearly on top of each other across the entire energy range, and at several energies the dual-scattering survival actually drops *below* the multiple-scattering value, reversing the ordering of Eq. (2).

The high-statistics ensemble for α-Al_2O_3 (150 000 trajectories per energy, three seeds of 50 000) places this observation on a quantitative footing; the results are gathered in Table I.

Across all five energies, the single-to-multiple contrast in α-Al_2O_3 stays in the narrow range $R_{s/m} = 1.11$–1.22—distinctly below the 1.5–2.2 range seen in the other three targets (Sec. III B). The dual-scattering charge fraction is

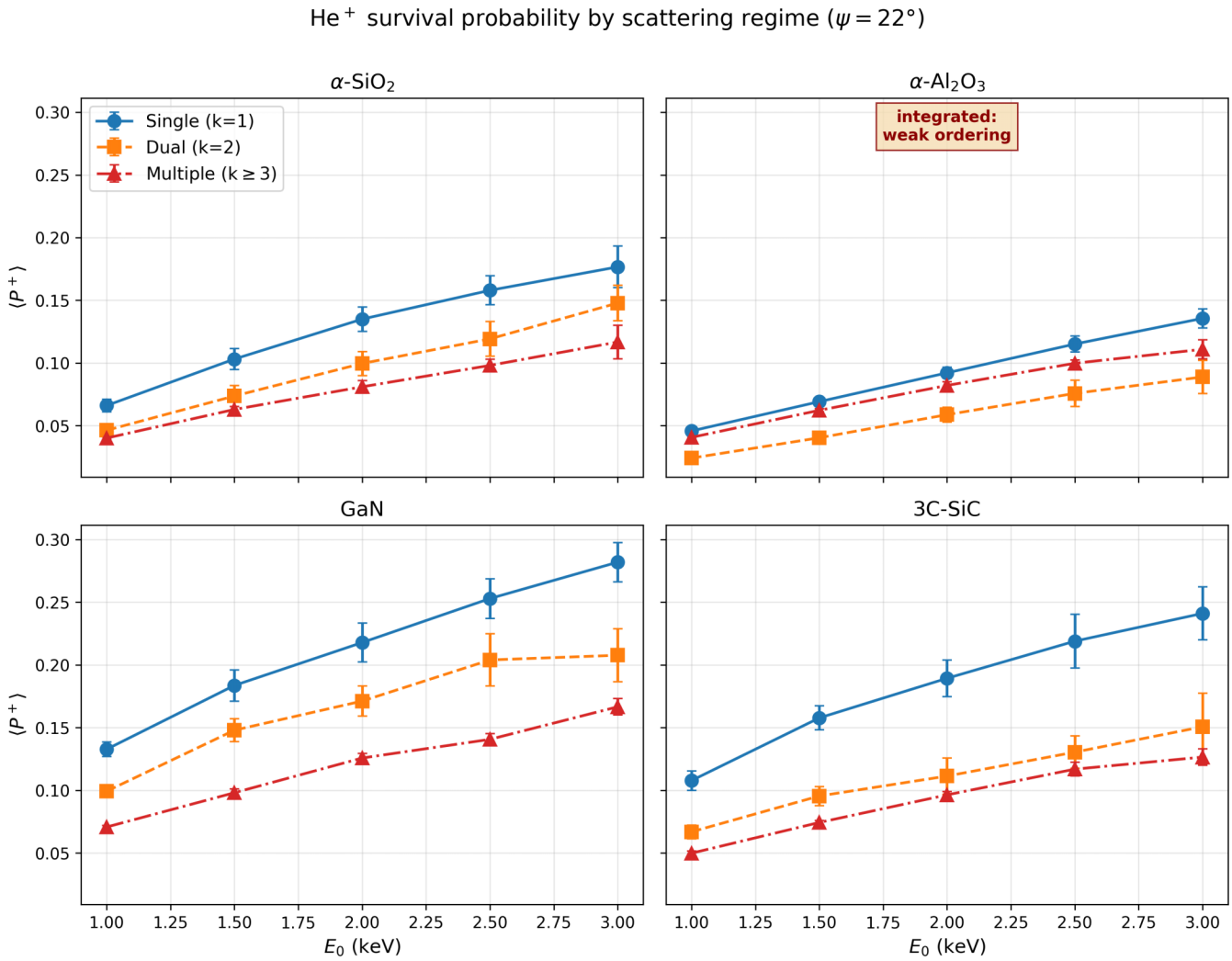


FIG. 2. Mean He^+ survival probability $\langle P^+\rangle$ vs incident energy E_0 for single, dual, and multiple scattering in the four targets ($\psi = 22^\circ$). For α-SiO_2, GaN, and 3*C*-SiC, the regime ordering $\langle P^+\rangle_s > \langle P^+\rangle_d > \langle P^+\rangle_m$ holds at all energies. In α-Al_2O_3, the integrated regime contrast becomes weak across the full energy range, an effect traced in Sec. III E to the sublattice-selective character of the underlying anomaly. Error bars are the standard error of the mean for each regime. Each panel pools three independent seeds, with $N = 20\,000$ trajectories per seed and energy for α-SiO_2, GaN, and 3*C*-SiC, and $N = 50\,000$ trajectories per seed and energy for α-Al_2O_3.

systematically smaller than the multiple-scattering one, the difference now reaching $4.5-21.5\sigma$ across the five energies in the pooled ensemble. The integrated effect, however, is not as strong as the dual-vs-multiple comparison might suggest.

TABLE I. Regime-resolved He^+ survival probabilities for α-Al_2O_3 at $\psi = 22^\circ$ from 150 000 trajectories per energy point (three independent seeds of 50 000 each, pooled). Errors in the last digit(s) are quoted in parentheses. The last column gives the statistical significance of $P_m - P_d > 0$ in standard deviations for the pooled ensemble.

E_0 (keV)	$\langle P^+\rangle_s$	$\langle P^+\rangle_d$	$\langle P^+\rangle_m$	$R_{s/m}$	sig. $(P_m - P_d)$
1.0	0.0457(7)	0.0241(7)	0.0407(3)	1.13	21.5σ
1.5	0.0691(13)	0.0403(15)	0.0622(6)	1.11	13.8σ
2.0	0.0921(19)	0.0588(24)	0.0821(10)	1.12	8.8σ
2.5	0.1151(26)	0.0759(35)	0.0998(16)	1.15	6.2σ
3.0	0.1356(33)	0.0886(45)	0.1110(22)	1.22	4.5σ

The reason, as shown below, is that the integrated signal averages over two opposing sublattice contributions that partially cancel each other.

D. Robustness checks

Before drawing conclusions from this anomaly, three independent checks were performed to rule out trivial origins.

(a) Neutralization-parameter sensitivity. The post-processing nature of the Hagstrum kernel made it cheap to recompute $\langle P^+\rangle$ for a $\pm 30\%$ scan around the base v_0, using the same backscattered ensemble and three values $v_0 = 0.7,\ 1.0$, and $1.3 \times v_0^{\text{base}}$. The absolute survival values shift, of course, in the direction Eq. (1) demands, but the ratio $\langle P^+\rangle_d / \langle P^+\rangle_m$ proves remarkably insensitive to v_0 (Fig. 3). At every energy the three curves lie strictly below unity—the ratio ranges from about 0.57–0.64 at 1 keV to about 0.77–0.84 at 3 keV across the full $\pm 30\%$ span of v_0—so the anomaly is present throughout and cannot be dismissed as a numerical accident of the chosen neutralization parameter.

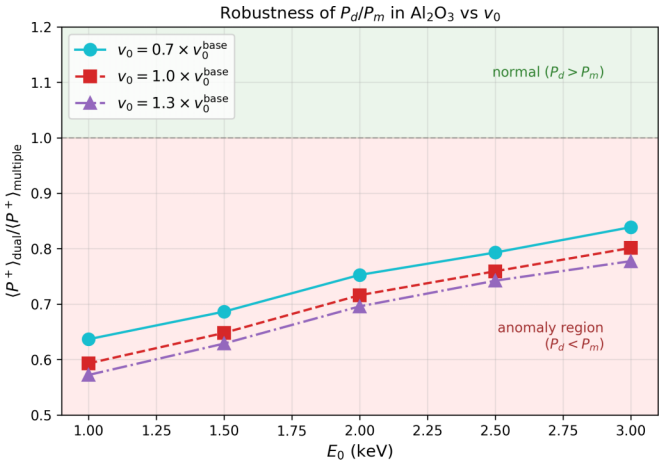


FIG. 3. Robustness of the α-Al_2O_3 anomaly: ratio $\langle P^+\rangle_d/\langle P^+\rangle_m$ as a function of incident energy for three values of the Hagstrum velocity parameter v_0, spanning $\pm 30\%$ around the base value $v_0^{base} = 3.3 \times 10^5$ m/s. The three curves are closely spaced and remain below unity at all energies, showing that the anomaly is not driven by the choice of v_0.

(b) Detector-window selection. A second concern is whether the inverted ordering survives the angular acceptance of a realistic detector. A detector cut was applied to the same pooled ensemble, selecting ions with $|\theta - 136^\circ| \leqslant 5^\circ$ (narrow ESA-LEIS window) and with $\leqslant 15^\circ$ (wide window). The resulting ratios are summarized in Table II. In the wide window, which retains 100–800 dual events per energy, the anomalous ordering $P_d < P_m$ survives at all five energies, with the ratio held between 0.66 and 0.71. In the much more restrictive narrow $\pm 5^\circ$ window the inversion is preserved at 1–1.5 keV ($P_d/P_m = 0.59$ and 0.79) but the surviving dual-event count drops to a few tens, so the ratio becomes statistics-limited above 2 keV and even rises above unity at 2.5 keV ($N_d = 33$). The wide-window result, together with the full no-cut ensemble, shows that the inversion is robust to realistic angular selection; a dedicated high-statistics campaign would be needed for a quantitative narrow-window analysis at the highest energies.

TABLE II. Detector-window scan of the dual/multiple ratio $\langle P^+\rangle_d/\langle P^+\rangle_m$ in α-Al_2O_3. "No cut" uses the full backscattered ensemble (150 000-trajectory pooled run, Table I). "Wide" and "narrow" apply $|\theta - 136^\circ| \leqslant 15^\circ$ and $\leqslant 5^\circ$ respectively to the same ensemble. N_d/N_m are the pooled numbers of dual- and multiple-scattering events surviving each cut. The anomaly $P_d/P_m < 1$ is present at every energy in the no-cut and wide-window columns; the narrow $\pm 5^\circ$ window retains few dual events and becomes statistics-limited above 2 keV.

E_0	No cut		Wide ($\pm 15^\circ$)		Narrow ($\pm 5^\circ$)	
(keV)	N_d/N_m	ratio	N_d/N_m	ratio	N_d/N_m	ratio
1.0	2509/19586	0.59	807/6121	0.70	226/2040	0.59
1.5	1315/9500	0.65	341/2825	0.71	87/883	0.79
2.0	799/5055	0.72	236/1521	0.71	56/491	0.88
2.5	536/2957	0.76	143/843	0.71	33/263	1.19
3.0	377/1663	0.80	100/485	0.66	29/145	0.83

TABLE III. Seed-to-seed reproducibility of the Al-sublattice inversion in α-Al_2O_3. The three production seeds (42, 1729, 271 828) at $N = 50\,000$ trajectories each, for all five energies. N_d^{Al} and N_m^{Al} count dual- and multiple-scattering events ending on Al; the per-seed significance (σ) is the $(P_m - P_d)/\sqrt{eP_d^2 + eP_m^2}$ statistic used in Table IV. The "pooled" row at each energy combines the three seeds (matching Table IV).

E_0 (keV)	seed	N_d^{Al}	N_m^{Al}	P_d/P_m	sig.
1.0	42	811	5330	0.59	11.5σ
1.0	1729	845	5168	0.62	10.9σ
1.0	271 828	789	5236	0.59	11.7σ
1.0	pooled	2445	15734	0.60	19.7σ
1.5	42	411	2462	0.73	5.3σ
1.5	1729	429	2470	0.62	8.1σ
1.5	271 828	428	2437	0.60	8.4σ
1.5	pooled	1268	7369	0.65	12.6σ
2.0	42	228	1289	0.70	5.0σ
2.0	1729	264	1325	0.76	3.9σ
2.0	271 828	268	1222	0.69	5.3σ
2.0	pooled	760	3836	0.72	8.2σ
2.5	42	166	713	0.66	5.0σ
2.5	1729	170	755	0.79	2.7σ
2.5	271 828	170	723	0.77	3.2σ
2.5	pooled	506	2191	0.74	6.3σ
3.0	42	126	398	0.79	2.3σ
3.0	1729	102	429	0.77	2.7σ
3.0	271 828	120	401	0.89	1.2σ
3.0	pooled	348	1228	0.81	3.7σ

(c) Seed-to-seed reproducibility. A natural concern, raised for the original low-statistics runs, is whether the inversion might be a favorable realization of the random-number generator. The present production removes this concern by construction: every energy point is computed independently for three random seeds (42, 1729, 271828) at $N = 50\,000$ trajectories each. Table III lists the per-seed Al-ending P_d/P_m and its significance at all five energies. Every one of the fifteen independent runs (five energies $\times$ three seeds) gives $P_d/P_m < 1$ on the Al sublattice (Fig. 4), and the per-seed ratios are tightly clustered—for example, 0.59–0.62 at 1 keV and 0.77–0.89 at 3 keV, a spread far smaller than the near factor-of-ten seed-to-seed scatter of the original 1000-trajectory runs. The per-seed significances range from $10.9-11.7\sigma$ at 1 keV down to $1.2-2.7\sigma$ at 3 keV, and the pooled three-seed ensemble (Table IV) reaches 19.7σ at 1 keV. The inversion is therefore a stable, reproducible feature of the corundum Al sublattice.

E. Sublattice decomposition

To localize the origin of the anomaly, the backscattered ensemble of α-Al_2O_3 was sliced by the chemical identity of the "final-collision atom"—that is, the atom involved in the last collision before exit. Figure 5 plots $\langle P^+\rangle_s$, $\langle P^+\rangle_d$, and $\langle P^+\rangle_m$ separately for Al-ending and O-ending trajectories.

The decomposition is clean. On the Al sublattice, the dual-scattering survival lies below the multiple-scattering value at every one of the five energies, with P_d/P_m rising

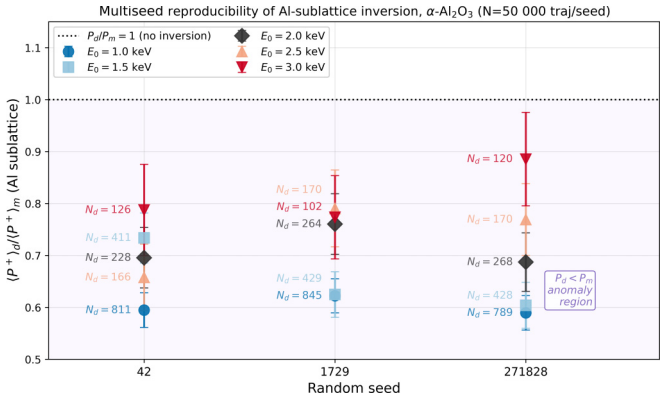


FIG. 4. Multiseed reproducibility of the Al-sublattice inversion. Per-seed dual/multiple ratio P_d/P_m (Al-ending trajectories) for the three production seeds (42, 1729, 271 828) at all five energies, $N = 50\,000$ trajectories per seed. The dotted horizontal line marks $P_d/P_m = 1$. Error bars are propagated from the per-regime SEM. All fifteen runs (five energies × three seeds) lie below unity, with a seed-to-seed spread far smaller than in the original low-statistics data.

monotonically from 0.60 at 1 keV to 0.81 at 3 keV; the strongest deviation is at 1 keV, where the pooled significance reaches 19.7σ ($10.9-11.7\sigma$ per seed). On the O sublattice, the conventional ordering is restored at all five energies, with $P_d/P_m = 1.27$–1.63; with the increased statistics, the O-ending dual-scattering channel is now well populated ($N_d \gtrsim 29$ per energy, summed over seeds). The full sublattice decomposition is collected in Table IV.

The reason the integrated anomaly of Fig. 2 appears weaker than the sublattice-resolved one becomes clear at this point. Al-ending trajectories dominate the backscattered population: across the 1–3 keV range, between 79% and 83% of backscattered ions terminate on Al, leaving only 17%–21% on O. The Al-sublattice contribution therefore controls the integrated regime ordering, and the partial cancellation against the (oppositely ordered) O-sublattice contribution explains why the integrated $P_m - P_d$ significances in Table I are smaller than the cleanly resolved Al-only values in Table IV.

TABLE IV. Sublattice-resolved P_d/P_m ratio in α-Al_2O_3 from 150 000 trajectories per energy (three independent seeds of 50 000 each, pooled). N is the number of backscattered ions ending on the indicated sublattice. The last column gives the statistical significance of the deviation from $P_d = P_m$ on the Al sublattice for the pooled ensemble; each seed individually gives $P_d < P_m$ (per-seed significances span 1.2-11.7σ, Table III).

E_0 (keV)	N_{Al}	$(P_d/P_m)_{Al}$	N_O	$(P_d/P_m)_O$	sig.$_{Al}$
1.0	21253	0.60	4316	1.40	19.7σ
1.5	10521	0.65	2479	1.40	12.6σ
2.0	5834	0.72	1471	1.45	8.2σ
2.5	3562	0.74	955	1.63	6.3σ
3.0	2225	0.81	585	1.27	3.7σ

TABLE V. Geometry and charge survival of dual-scattering collision-pair types in α-Al_2O_3, pooled over all five incident energies and three seeds (150 000 trajectories per energy). $\langle|\Delta z|\rangle$ is the average vertical separation between the two collision atoms, $\langle\Delta r_{lat}\rangle$ the average lateral separation, $\langle P^+\rangle$ the average He^+ survival probability of the dual trajectory.

Pair	N	$\langle\|\Delta z\|\rangle$ (Å)	$\langle\Delta r_{lat}\rangle$ (Å)	$\langle P^+\rangle$
Al–Al	3711	0.29	3.63	0.024
O–Al	1616	1.11	2.52	0.074
O–O	134	1.44	5.93	0.126
Al–O	75	1.32	4.99	0.129

F. Trajectory topology and collision-pair geometry

What does the geometry of those Al-ending dual trajectories actually look like? To find out, the full 3D coordinates of the first and second collision atoms were recorded for every dual-scattering trajectory in the production runs (three seeds of 50 000 trajectories per energy), and the records were grouped by the chemical identity of the colliding pair—Al-Al, Al-O (with the ion hitting Al first and O second), O-Al, or O-O. The structural features of corundum that underlie this geometry—the buckled Al sheets, their ∼2.16 Å interlayer spacing, and the in-plane Al-Al neighbor shells—are summarized in Fig. 6, which provides a three-dimensional reference for the distances quoted below. The result, summarized in Fig. 7 and Table V, can be summarized in three observations.

(1) *Al-Al pairs are in-plane.* Averaged across all five energies, the mean vertical separation between the two collision atoms in an Al-Al pair is $\langle|\Delta z|\rangle = 0.29$ Å. This is small compared with the interlayer separation of Al planes in corundum (∼2.16 Å between adjacent Al a–b sheets), so the two collision atoms belong to the same Al sheet of the corundum structure—the spatial distribution is decisively not random. This classification is set by the corundum lattice topology and does not rely on the precise value of the thermal-displacement amplitude.

(2) *Al-Al lateral spacings match corundum.* The per-trajectory data at 2 keV (Fig. 7(a) split into three clean clusters at $\Delta r_{lat} \approx 2.6$, 4.7 and 7.1 Å. All three correspond to *in-plane* Al-Al neighbor shells of corundum, computed from the same lattice parameters used in the simulation ($a = 4.759$ Å, $c = 12.991$ Å): the first shell at 2.75 Å (multiplicity 3, buckled by $|\Delta z| = 0.49$ Å), the second at 4.76 Å (multiplicity 6, perfectly in-plane), and the fourth at 7.27 Å (multiplicity 6, buckled). The intermediate third shell at 5.50 Å has half the multiplicity and lies close to the second-shell tail, so it appears as a shoulder rather than a resolved cluster. The clustering is not a numerical artifact but a direct fingerprint of the directional Al-Al network within the *a*-*b* plane.

(3) *Al-Al pairs dominate the channel and have the lowest survival.* Al-Al pairs make up the majority of the backscattered dual-scattering events in α-Al_2O_3: their share falls monotonically from 72% at 1 keV to 52% at 3 keV (72%, 70%, 61%, 58%, 52% at 1, 1.5, 2, 2.5, 3 keV; 67% pooled over all energies), the exact fractions being labeled inside the bars of Fig. 7(c). The decrease tracks the shift from grazing

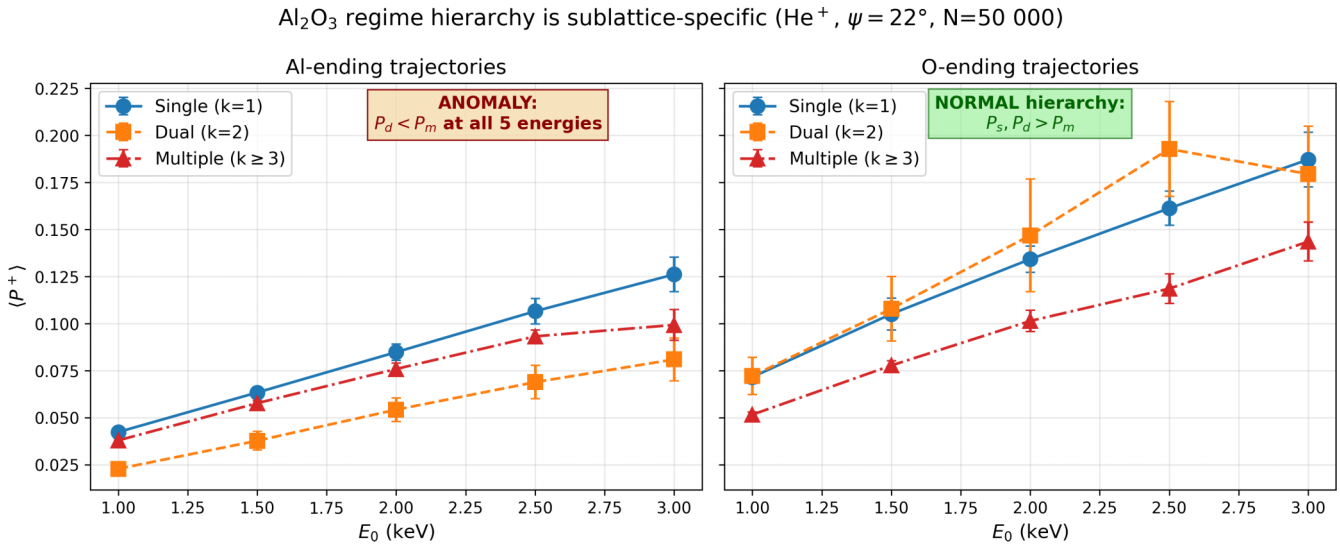


FIG. 5. Sublattice-resolved He^+ survival probabilities in α-Al_2O_3. (Left) Trajectories whose final collision is on an Al atom. (Right) Trajectories whose final collision is on an O atom. The Al sublattice shows the inverted ordering $\langle P^+ \rangle_d < \langle P^+ \rangle_m$ at all five energies, with a per-seed significance ranging from 1.2σ at 3 keV to 11.7σ at 1 keV (highest where the counts are largest). The O sublattice follows the standard $\langle P^+ \rangle_s > \langle P^+ \rangle_d > \langle P^+ \rangle_m$ ordering at all five energies. With the increased statistics every energy is now populated on both sublattices; in particular, the $E_0 = 2.5$ keV Al dual-scattering point, empty in the original submission, now contains ≈170 events per seed. Each panel uses $N = 50\,000$ trajectories per seed, pooled over three seeds. Uncertainties are per-regime standard errors of the mean, added in quadrature for the significance.

near-planar trajectories at low energy, for which the in-plane Al–Al geometry is maximally accessible, to steeper trajectories at higher energy. Al-Al pairs also have the lowest charge survival: their mean, $\langle P^+ \rangle_{\text{Al-Al}} = 0.024$, is a factor of 3.3 below that of all other pair types combined [$\langle P^+ \rangle_{\text{others}} = 0.080$, Fig. 7(c)]. It is these in-plane Al-Al events that carry the integrated α-Al_2O_3 regime anomaly.

With this in hand, the physical picture is straightforward. In corundum, the Al cations occupy two-thirds of the octahedral sites within the *a*-*b* planes interleaved between hcp oxygen layers, so each in-plane Al has well-defined Al neighbors at 2.75, 4.76, and 7.27 Å. A grazing He^+ projectile that hits one of these cations can be redirected, with non-negligible probability, toward an in-plane Al neighbor at one of these

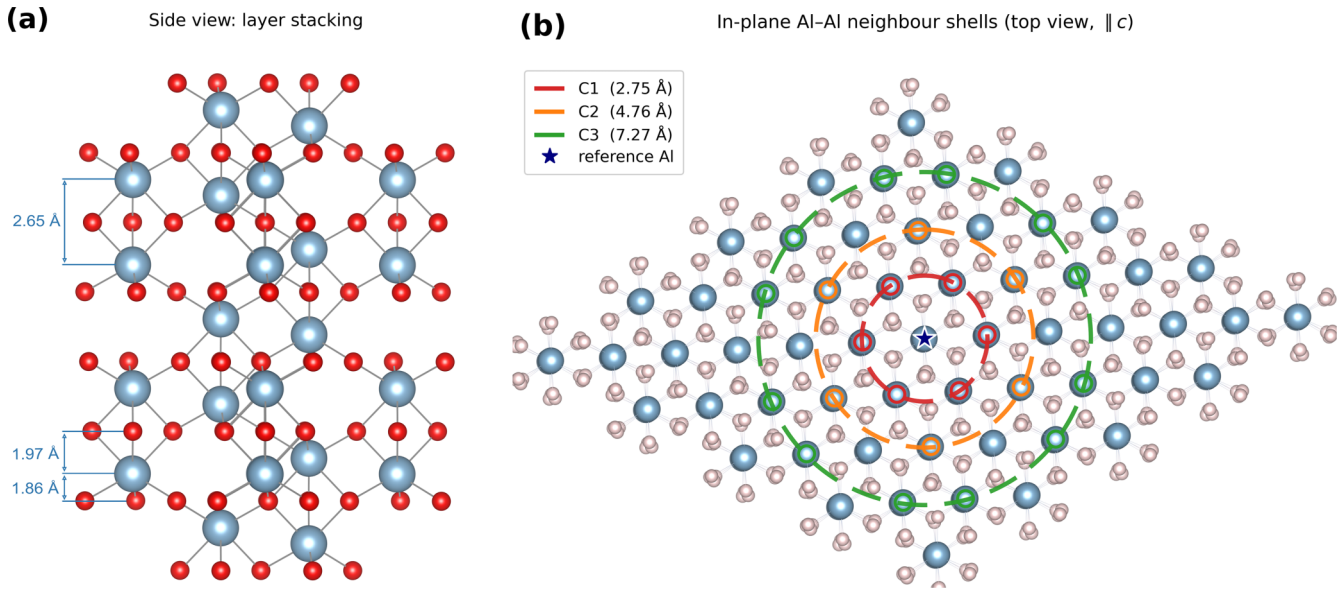


FIG. 6. Crystal structure of corundum (α-Al_2O_3, space group R$\bar{3}$c; $a = 4.759$ Å, $c = 12.991$ Å, the experimental values used in the simulation; Al blue, O red), rendered with VESTA [32]. (a) Side view of the layer stacking, with the nearest vertical Al-Al distance (2.65 Å) and the two octahedral Al–O bond lengths (1.86 and 1.97 Å) marked. (b) Top view along [0001], with the three in-plane Al-Al neighbor shells drawn as rings around a reference Al: C1 at 2.75 Å (shell 1), C2 at 4.76 Å (shell 2), and C3 at 7.27 Å (shell 4). These three shells generate the clusters C1-C3 of Fig. 7(a); the weak intermediate shell 3 (5.50 Å) is omitted for clarity.

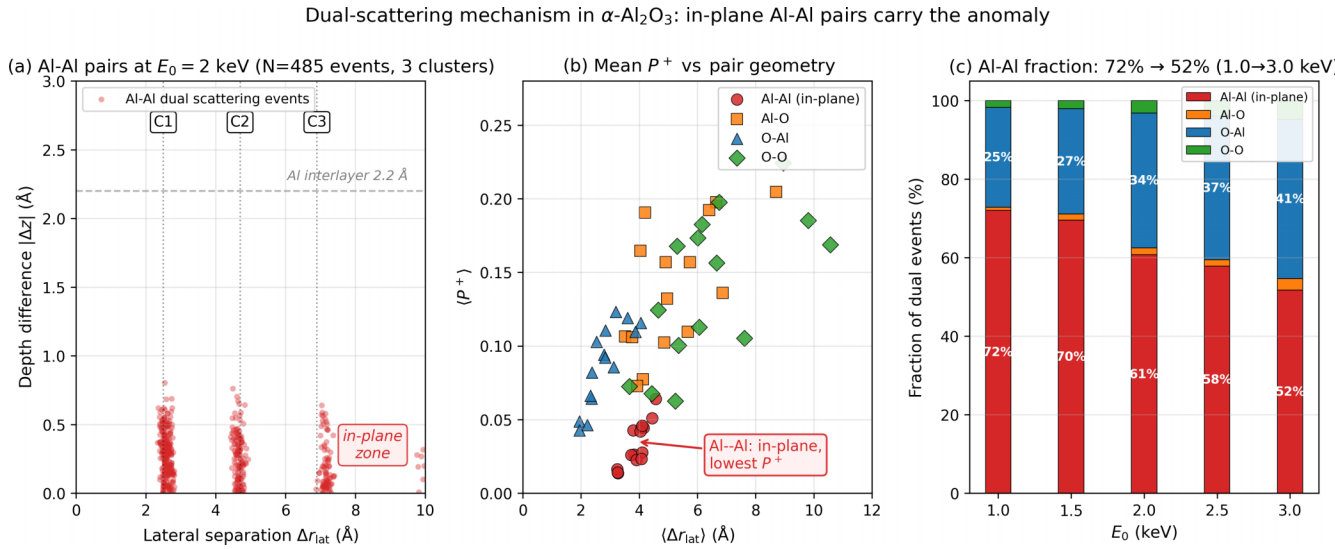


FIG. 7. Microscopic mechanism of the α-Al_2O_3 regime anomaly. (a) Per-trajectory geometry of dual-scattering events at $E_0 = 2$ keV in the plane of vertical separation $|\Delta z|$ vs lateral separation $\Delta r_{\rm lat}$ between the two collision atoms. Al-Al pairs cluster strictly in the in-plane region ($|\Delta z| < 0.7$ Å) at three lateral spacings of 2.6, 4.7, and 7.1 Å, matching the first, second, and fourth in-plane Al-Al neighbor shells of corundum. O-Al pairs occupy the interlayer region ($|\Delta z| \geqslant 0.6$ Å). (b) Mean He^+ survival probability $\langle P^+ \rangle$ of each dual-scattering pair type plotted against its mean lateral separation $\langle \Delta r_{\rm lat} \rangle$. The in-plane Al-Al pairs (filled circles) have the lowest survival of all four pair types, well below the O-Al, Al-O, and O-O pairs. (c) Mean He^+ survival probability for dual-scattering events, decomposed by collision-pair type. Al-Al pairs give the lowest charge survival ($\langle P^+ \rangle = 0.024$), a factor of 3.3 below the mean of all other pair types ($\langle P^+ \rangle = 0.080$). The bar labels give the percentage of dual-scattering events of each pair type at each energy; Al-Al pairs make up 52%–72% of the channel (Table V).

characteristic distances—without descending into the next O layer below. The resulting dual trajectory then travels nearly parallel to the surface for some 3–5 Å between the two collisions, sampling the high-density electron region of the topmost atomic plane for an unusually extended time. In the velocity-dependent neutralization picture of Eq. (1), this prolonged in-plane residence reduces $v_\perp$ at the second collision (the in-plane motion does not change v_z) and enhances neutralization. The net result is a P^+ smaller than that of the multiple-scattering ions, which descend more steeply through the surface and exit faster.

The other three pair types (O-Al, Al-O, O-O) involve at least one inter-layer hop and therefore do not display the in-plane geometry. Their charge survival is comparable to or above the multiple-scattering channel, and they follow the standard regime ordering. With Al-Al pairs accounting for 52%–72% of all dual events depending on energy (67% pooled), the Al-sublattice anomaly seen in Fig. 5 dominates the integrated regime ordering shown in Fig. 2.

IV. DISCUSSION

A. A taxonomy of regime hierarchies

Stepping back from the corundum case, the present results combined with those of Brötzner *et al.* [11] suggest that He^+ LEIS charge-fraction hierarchies fall into at least three distinct classes, organized by surface crystal topology rather than by chemical identity.

(1) *Strong hierarchy* ($R_{s/m} \sim 10$, *normal ordering*). Observed in $CaSiO_3$ [11]. Likely a feature of mixed-cation silicates built on open three-dimensional networks, where single, dual, and multiple scattering trajectories carve out very different effective transit times through the surface electron density.

(2) *Moderate hierarchy* ($R_{s/m} = 1.5$–2.2, *normal ordering*). Found here in α-quartz SiO_2, wurtzite GaN, and zincblende 3*C*-SiC. Characteristic of moderately dense compound oxides and of tetrahedrally coordinated wide-band-gap semiconductors. The basic ordering is preserved, but the contrast is muted relative to $CaSiO_3$.

(3) *Sublattice-selective hierarchy* (*integrated* $R_{s/m} \sim 1$; $P_d < P_m$ *on the dominant cation sublattice; normal ordering on the anion sublattice*). The case of α-Al_2O_3. Probably a generic feature of dense corundumlike oxides with directional in-plane cation networks resting on hcp anion sublattices.

It is worth emphasizing what this classification is and is not. It is not a classification by electronic class. α-quartz and α-Al_2O_3 are both wide-band-gap dielectric oxides with nearly identical band gaps (~8.8 and ~8.7 eV, respectively), yet they fall in different categories. Conversely, the moderate-hierarchy class spans both an oxide (α-quartz) and two semiconductors (GaN, 3*C*-SiC). The defining property is structural—specifically, whether the dominant dual-scattering pathway remains within the topmost atomic plane or descends to the next layer below. Once in-plane pathways begin to dominate the dual-scattering channel, as they do in α-Al_2O_3, the regime hierarchy breaks in the manner laid out in Sec. III F.

B. Implications for quantitative LEIS analysis

The standard quantitative LEIS expression relates the measured He^+ intensity from element α to the surface concentration of that element through a scattering cross section, a kinematic factor, an instrumental factor, and an effective

TABLE VI. Qualitative consistency check of the present BCA simulations against published LEIS observations. The comparison is at the level of trends and orders of magnitude; absolute spectrum-level agreement is not claimed.

Observable	This work	Literature
He^+ ESA-LEIS yield (oxides, 1–3 keV)	1.8%–17% (Fig. 1)	5%–15% [8]
Dominant final-collision atom in GaN	Ga (dominant final-collision atom)	Ga-dominated [19,20]
Si and C distinct in 3*C*-SiC	distinct populations	mass-resolved Si/C peaks
SiO_2 vs Al_2O_3 yield ratio (1 keV)	$Y_{Al_2O_3}/Y_{SiO_2} \approx 1.4$	denser oxide → larger yield [2]
Single/multiple $\langle P^+ \rangle$ contrast in silicate	$R_{s/m} \approx$ 1.5-1.7 (α-SiO_2)	$R_{s/m} \sim 10$ in $CaSiO_3$ [11]

charge fraction ξ_α. Brötzner *et al.* [11] argued that this fraction should be split by collision count,

$$I(E) = \xi_s I_s^{\mathrm{BCA}}(E) + \xi_d I_d^{\mathrm{BCA}}(E) + \xi_m I_m^{\mathrm{BCA}}(E), \qquad (3)$$

with the implicit Brötzner ordering $\xi_s > \xi_d > \xi_m$. The α-Al_2O_3 result just discussed shows that this decomposition, useful as it is, is not enough whenever the dual-scattering channel turns sublattice-selective. An extended form is proposed instead,

$$I(E) = \sum_\alpha \sum_k \xi_{\alpha,k}\, I_{\alpha,k}^{\mathrm{BCA}}(E), \qquad (4)$$

in which α runs over the chemical identity of the final-collision atom and k over the collision-count regime. Within each sublattice the standard regime ordering is largely restored (modulo the $E_0 = 1$ keV behavior, where strong neutralization tends to dominate all channels): one finds $\xi_{O,s} > \xi_{O,d} > \xi_{O,m}$ in α-Al_2O_3, and similar normal orderings on both sublattices of α-SiO_2, GaN, and 3*C*-SiC. The integrated apparent anomaly in corundum then traces back unambiguously to the Al-sublattice contribution, which itself violates the regime ordering for the geometric reasons set out in Sec. III F.

A practical consequence is that effective charge fractions calibrated on a reference compound cannot be transferred between materials with different lattice topology, even when the chemical identity of the target atom is the same. The ξ value extracted for Al from α-Al_2O_3 should not be transported to a less-dense aluminosilicate or to a metallic Al surface; conversely, a universal Al ξ obtained from metallic-Al reference data is liable to under- or overestimate Al concentrations in corundumlike oxides because the in-plane Al-Al pathway that dominates corundum has no analog in the fcc Al metal.

C. Comparison with experiment

The simulations reported here are not intended as a direct fit to a specific ESA-LEIS measurement. A quantitative spectrum-level comparison would require a detector-calibrated angular acceptance, the ion-beam energy spread, and an experimental run at the matching $\psi = 22^\circ$ grazing geometry. What is offered instead is a set of qualitative consistency checks against published LEIS data on the four target materials, summarized in Table VI.

The yield range is consistent with the published ESA-LEIS scale on oxides [8]; the dominance of Ga-ending trajectories in GaN matches the experimental observation of Ga-dominated LEIS spectra [19,20]; and the existence of a Si/C sublattice contrast in 3*C*-SiC follows from the LEIS mass resolution between Si ($m = 28$) and C ($m = 12$), which produces well-separated peaks. The present α-SiO_2 regime contrast ($R_{s/m} \approx$ 1.5–1.7) is weaker than the near-order-of-magnitude contrast reported for $CaSiO_3$ [11], which is internally consistent with the denser anion sublattice of α-quartz relative to the open silicate framework of $CaSiO_3$ (Sec. III B).

The most direct test of the in-plane Al–Al mechanism proposed in Sec. III F would be a sublattice-resolved high-resolution ESA-LEIS spectrum of α-$Al_2O_3(0001)$ at $E_0 \approx 1$ keV under grazing incidence. The mechanism predicts that the Al peak in such a spectrum should display a low-energy shoulder or tail attributable to the in-plane dual-scattering channel, with intensity reduced relative to the kinematic expectation by approximately the Al-sublattice factor $P_d/P_m \approx 0.6$ identified here. It is hoped that the present results will encourage such a measurement.

D. Limitations

A handful of caveats deserve explicit mention.

(a) Polytype dependence in SiC. Only 3*C*-SiC was computed. The 4H and 6H polytypes share its local atomic packing closely and should behave qualitatively the same, but quantitative shifts in $\langle|\Delta z|\rangle$ for the dual-scattering channel are plausible because of the rumpling that stacking faults induce.

(b) GaN polarity. Attention was restricted to the ideal Ga-terminated (0001) face. The N-terminated surface—accessible by mechanical polishing or preferential etching—may exhibit a different sublattice asymmetry, since the N–N second-neighbor distances differ from the Ga–Ga ones.

(c) Detector statistics at high energy. The detector-resolved analysis becomes statistics-limited above ∼2.5 keV only in the narrow $\pm 5^\circ$ window, where a few tens of dual-scattering events survive the cut; the wide $\pm 15^\circ$ window remains well populated (100–800 dual events per energy) and preserves the inversion at all energies. An even larger campaign would sharpen the narrow-window high-energy points for a fully detector-resolved comparison with experiment at the upper end of the energy range.

(d) Hagstrum kernel. Equation (1) is an effective trajectory-level kernel, not a microscopic description of all charge-exchange channels. More refined treatments that include explicit close-collision reionization and Auger pathways [9,25,27] would shift the absolute P^+ values, though the regime ordering itself is demonstrably independent of the kernel parameter within ±30% (Sec. III D). The absolute values of $\langle P^+ \rangle$ should accordingly be regarded as uncertain at the factor-of-two level until they are calibrated against an experimental reference.

(e) Polymorph choice. Real LEIS-relevant SiO_2 surfaces are usually amorphous or partially hydroxylated, whereas the present simulation used α-quartz. The qualitative result (moderate hierarchy, $R_{s/m} \sim 2$) is expected to survive; quantitative shifts of order 10%–20% on absolute yields cannot be excluded.

V. CONCLUSIONS

This work has presented scattering-regime-resolved BCA simulations of He^+ low-energy ion scattering from four crystalline targets—α-quartz SiO_2, corundum α-Al_2O_3, wurtzite GaN, and zincblende 3*C*-SiC—at grazing incidence ($\psi = 22^\circ$) over the 1–3 keV range. The calculations combined pair-specific Nordlund-Lehtola-Hobler interatomic potentials, position-dependent electronic stopping, Debye thermal vibrations, and a velocity-dependent Hagstrum-type neutralization kernel, with statistically converged trajectory ensembles for the high-statistics analysis.

For α-quartz SiO_2, GaN, and 3*C*-SiC the standard regime hierarchy $\langle P^+\rangle_{\text{single}} > \langle P^+\rangle_{\text{dual}} > \langle P^+\rangle_{\text{multiple}}$ holds at every investigated energy, with single-to-multiple contrast $R_{s/m} \approx$ 1.5-2.2. This represents a moderate version of the strong hierarchy reported for $CaSiO_3$ [11]. In α-Al_2O_3, on the other hand, the integrated regime hierarchy becomes weak ($R_{s/m} =$ 1.11–1.22) across the entire 1–3 keV range, and the ordering of P_d relative to P_m is reversed. This integrated effect originates from the dominant Al sublattice, on which $P_d < P_m$ holds at all five energies and for all three seeds, with a pooled sublattice-resolved significance reaching 19.7σ at 1 keV ($10.9-11.7\sigma$ per individual seed). The inversion is robust to a $\pm 30\%$ variation of the Hagstrum velocity parameter, survives detector-window selection, and reproduces across independent random seeds.

Decomposition by final-collision atom further shows that the anomaly is sublattice-selective: Al-ending trajectories give $P_d < P_m$ at all energies, while O-ending trajectories follow the normal ordering. Since the Al sublattice carries 79%–83% of the backscattered intensity across the 1–3 keV range, the Al-ending events control the integrated ordering. Geometric analysis of the recorded collision-pair coordinates resolves the microscopic mechanism. Between 52% and 72% of the dual-scattering events in α-Al_2O_3 (67% pooled over energy, rising toward low energy) involve two Al atoms in the same atomic layer ($\langle|\Delta z|\rangle = 0.29$ Å, small compared with the $\sim$2.2 Å Al-Al interlayer separation in corundum), with lateral separations clustered at 2.6, 4.7, and 7.1 Å—the first, second, and fourth in-plane Al-Al neighbor distances of corundum. The prolonged lateral residence of these in-plane trajectories in the surface electron density enhances neutralization and suppresses P^+ below that of the deeper, shorter-residence multicollision events.

The practical implication is that quantitative regime-resolved LEIS analysis of compound oxides should employ a regime-by-sublattice decomposition $\xi_{\alpha,k}$ [Eq. (4)] rather than a regime-only or sublattice-only effective fraction; within each sublattice the standard ordering is largely restored. The broader picture that emerges is one in which the structural regularities of the target lattice can carve out specific scattering pathways that override the generic regime hierarchy expected from the velocity dependence of the neutralization kernel alone. Together with the recent $CaSiO_3$ result of Brötzner *et al.*, the present analysis points to a quantitative interpretation of He^+ LEIS spectra that must be material-specific in a structurally informed way—built on lattice topology, not on collision count or chemistry alone.

ACKNOWLEDGMENTS

The author thanks U. O. Kutliev (Urgench State University) for discussions on ion-surface scattering simulations and for collaboration on related work on grazing-incidence ion scattering from oxide surfaces.

DATA AVAILABILITY

There are no publicly available research data or software supporting this manuscript. Requests for further information or data should be sent to the author.

APPENDIX: TABULATED DATA

This Appendix collects the numerical values underlying the figures of the main text, following the referee's suggestion to keep the running text uncluttered. The tables reproduce the data plotted in Figs. 2–5, and 7.

[1] H. Niehus, W. Heiland, and E. Taglauer, Low-energy ion scattering at surfaces, Surf. Sci. Rep. **17**, 213 (1993).

[2] H. H. Brongersma, M. Draxler, M. de Ridder, and P. Bauer, Surface composition analysis by low-energy ion scattering, Surf. Sci. Rep. **62**, 63 (2007).

[3] C. V. Cushman *et al.*, Low energy ion scattering (LEIS). A practical introduction to its theory, instrumentation, and applications, Anal. Methods **8**, 3419 (2016).

[4] S. Průša *et al.*, A practical guide to interpreting low energy ion scattering (LEIS) spectra, Appl. Surf. Sci. **657**, 158793 (2024).

[5] M. Draxler, R. Gruber, H. H. Brongersma, and P. Bauer, Velocity scaling of ion neutralization in low energy ion scattering, Phys. Rev. Lett. **89**, 263201 (2002).

[6] S. N. Markin, D. Primetzhofer, J. E. Valdés, E. Taglauer, and P. Bauer, Neutralization of low energy He^+ ions by Cu in the Auger regime, Nucl. Instrum. Methods Phys. Res. B **258**, 18 (2007).

[7] D. Primetzhofer, S. N. Markin, J. I. Juaristi, E. Taglauer, and P. Bauer, Crystal effects in the neutralization of He^+ ions in the low energy ion scattering regime, Phys. Rev. Lett. **100**, 213201 (2008).

[8] B. Bruckner, P. Bauer, and D. Primetzhofer, Neutralization of slow helium ions scattered from single crystalline aluminum

and tantalum surfaces and their oxides, Surf. Sci. **691**, 121491 (2020).

[9] A. Iglesias-García, F. Bonetto, R. Vidal, J. Ferrón, and E. C. Goldberg, Ion neutralization and high-energy electron emission in He^+ scattering by a highly oriented pyrolitic graphite surface, Phys. Rev. A **89**, 042702 (2014).

[10] P. F. Buitrago, M. A. Romero, C. J. Bonin, Y. Irusta, C. Gonzalez, R. Vidal, E. A. Garcia, and F. Bonetto, Neutralization of low-energy Ne^+ colliding with MoS_2 and metallic molybdenum: An experimental and theoretical study, Phys. Rev. A **110**, 012806 (2024).

[11] J. Brötzner, M. Kogler, P. S. Szabo, L. Kalchgruber, A. Nenning, A. Mutzke, H. Hofsass, M. Valtiner, and R. A. Wilhelm, Toward quantitative low-energy ion scattering on $CaSiO_3$ from comparison to multiple-scattering-resolved dynamical binary collision approximation simulations, Phys. Rev. B **113**, 075405 (2026).

[12] A. S. Ashirov, M. K. Qurbanov, I. U. Tangribergenov, M. K. Karimov, and K. U. Otabaeva, Inelastic energy loss of Ar ions scattered Al_2O_3 surface under grazing incidence, Phys. Chem. Solid State **22**, 255 (2021).

[13] A. S. Ashirov, U. O. Kutliev, S. Xakimov, and S. K. Ismailov, Low energy Ar^+ ions scattering from SiO_2 (001)$\langle\bar{1}10\rangle$ surface under grazing incidence, Mater. Sci. Forum **1049**, 152 (2022).

[14] U. O. Kutliev, A. S. Ashirov, G. X. Allayarova, and A. Saidova, Studies of implantation of O^+ ions into SiO_2(001) films at the small-angle ion bombardment, East Eur. J. Phys. **2**, 320 (2025).

[15] E. Ntemou, R. Holeňák, and D. Primetzhofer, Energy deposition by H and He ions at keV energies in self-supporting, single crystalline SiC foils, Radiat. Phys. Chem. **194**, 110033 (2022).

[16] R. Holeňák, E. Ntemou, S. Lohmann, M. Linnarsson, and D. Primetzhofer, Assessing trajectory-dependent electronic energy loss of keV ions by a binary collision approximation code, Phys. Rev. Appl. **21**, 024048 (2024).

[17] V. M. Fomin, V. R. Misko, J. T. Devreese, and H. H. Brongersma, Comparative analysis of the low-energy He^+ ions scattering on Al and Al_2O_3 surfaces, Nucl. Instrum. Methods Phys. Res. B **145**, 545 (1998).

[18] G. C. van Leerdam and H. H. Brongersma, Shielding effects in oxides studied by low-energy ion scattering, Surf. Sci. **254**, 153 (1991).

[19] M. M. Sung, J. Ahn, V. Bykov, J. W. Rabalais, D. D. Koleske, and A. E. Wickenden, Composition and structure of the GaN(000$\bar{1}$)-(1 × 1) surface, Phys. Rev. B **54**, 14652 (1996).

[20] J. Ahn, M. M. Sung, J. W. Rabalais, D. D. Koleske, and A. E. Wickenden, Surface composition and structure of GaN epilayers on sapphire, J. Chem. Phys. **107**, 9577 (1997).

[21] K. Abe, M. Sumitomo, T. Sumi, O. Eryu, and K. Nakashima, Effects of surface treatments of 6H-SiC upon metal-SiC interfaces, Mater. Sci. Forum **389-393**, 909 (2002).

[22] K. Nordlund, S. Lehtola, and G. Hobler, Repulsive interatomic potentials calculated at three levels of theory, Phys. Rev. A **111**, 032818 (2025).

[23] K. Nordlund, S. Lehtola, and G. Hobler, Erratum: Repulsive interatomic potentials calculated at three levels of theory, Phys. Rev. A **112**, 059901(E) (2025).

[24] P. M. Wolf, E. Pitthan, and D. Primetzhofer, Experimentally determined interatomic potentials in low-energy atomic collisions relevant for nuclear fusion, Phys. Rev. A **111**, 042812 (2025).

[25] M. Draxler, J. E. Valdés, R. Beikler, and P. Bauer, On the extraction of neutralisation information from low energy ion scattering spectra, Nucl. Instrum. Methods Phys. Res. B **230**, 290 (2005).

[26] D. Primetzhofer, M. Spitz, E. Taglauer, and P. Bauer, Resonant charge transfer in low-energy ion scattering: Information depth in the reionization regime, Surf. Sci. **605**, 1913 (2011).

[27] D. Goebl, B. Bruckner, D. Roth, C. Ahamer, and P. Bauer, Low-energy ion scattering: A quantitative method? Nucl. Instrum. Methods Phys. Res. B **354**, 3 (2015).

[28] M. T. Robinson and I. M. Torrens, Computer simulation of atomic-displacement cascades in solids in the binary-collision approximation, Phys. Rev. B **9**, 5008 (1974).

[29] J. P. Biersack and L. G. Haggmark, A Monte Carlo computer program for the transport of energetic ions in amorphous targets, Nucl. Instrum. Methods **174**, 257 (1980).

[30] J. F. Ziegler, J. P. Biersack, and U. Littmark, *The Stopping and Range of Ions in Solids* (Pergamon, New York, 1985).

[31] L.-M. Peng, G. Ren, S. L. Dudarev, and M. J. Whelan, Debye-Waller factors and absorptive scattering factors of elemental cryst., Acta Cryst. A **52**, 456 (1996).

[32] K. Momma and F. Izumi, *VESTA 3* for three-dimensional visualization of crystal, volumetric and morphology data, J. Appl. Cryst. **44**, 1272 (2011).